Glass-Ceramic Lithium Thiophosphate Electrolytes with Enhanced Conductivity and (Chemo)mechanical Properties for All-Solid-State Batteries

Jingui Yang,[a] Mareen Schaller,[b] Gennady Cherkashinin,[c] Ruizhuo Zhang,[a] Sylvio Indris,[b,d] Daniel Alves Dalla Corte,[e] Aleksandr Kondrakov,[a, f] Torsten Brezesinski,[a] and Florian Strauss[a,*]

[a]Battery and Electrochemistry Laboratory (BELLA), Institute of Nanotechnology, Karlsruhe Institute of Technology (KIT), Kaiserstr. 12, 76131 Karlsruhe, Germany.
[b]Institute for Applied Materials–Energy Storage Systems, Karlsruhe Institute of Technology (KIT), Kaiserstr. 12, 76131 Karlsruhe, Germany.
[c]Institute for Materials Science, Technical University Darmstadt, Peter-Grünberg-Str.2, 64287 Darmstadt, Germany.
[d]Applied Chemistry and Engineering Research Centre of Excellence (ACER CoE), Universite Mohammed VI Polytechnique (UM6P), Lot 660, Hay Moulay Rachid, Ben Guerir, 43150, Morocco.
[e]Sphere Energy SAS, 250 Bis Boulevard Saint Germain, 75007 Paris, France.
[f]BASF SE, Carl-Bosch-Str. 38, 67056 Ludwigshafen, Germany.
*Email: florian.strauss@kit.edu

Abstract

Solid-state batteries (SSBs) based on inorganic solid electrolytes (SEs) possibly offer enhanced energy and power densities, along with increased safety compared to state-of-the-art rechargeable batteries using liquid organic electrolytes. However, the stiffness and brittle nature of inorganic SEs can complicate cell fabrication and lead to (chemo)mechanical failure of SSBs during operation. In the past, the design of SEs has mainly focused on optimizing ionic conductivity and (electro)chemical stability. However, to mitigate detrimental (chemo)mechanical degradation in SSBs, due to electrode volume and morphology changes upon charge and discharge, the mechanical properties of SEs also need to be considered in their development. In this regard, glass-ceramic SEs offer a reduced hardness, but often suffer from rather low ionic conductivities. Herein we systematically investigate the effect of LiI additive and

annealing temperature on phase composition and charge transport properties of a series of SEs with the general composition of $4.25Li_2S{-}0.75P_2S_5{-}1.5SiS_2{-}xLiI$ ($0 \leq x \leq 2$). We demonstrate that the glass-ceramic material (LPSI-GC) with x(LiI) = 1.25 achieves a high room-temperature ionic conductivity of 4.38 mS cm^{-1} and further exhibit favorable mechanical properties owing to the combination of crystalline *t*-$Li_{10.5}P_{1.5}Si_{1.5}S_{12}$ and I-rich amorphous phases. When implemented in SSBs together with a layered Ni-rich oxide cathode material, the LPSI-GC SE enables stable cycling for over 100 cycles although (electro)chemical decomposition, detected by X-ray photoelectron spectroscopy, is evident. Collectively, our results demonstrate that glass-ceramic SEs allow for simultaneous optimization of ionic conductivity and mechanical properties, thus enabling long-term SSB operation.

Introduction

Solid-state batteries (SSBs) are emerging as a promising technology for next-generation energy storage systems, offering enhanced safety as well as high energy and power densities.[1] The rigid nature of solid electrolytes (SEs) entails the potential to employ Li metal anodes by effectively suppressing dendrite growth and further enables bipolar stacking configurations, significantly increasing the active material content in batteries.[2] When paired with cathode active materials (CAMs) like sulfur or layered Ni-rich oxides, SSBs are well-positioned to meet the growing demands for electric transportation and portable electronics.[3,4] These promising prospects have fueled intense research efforts in both academia and industry to advance this technology, with a major focus currently being on the development of high-performance SEs. Despite their advantages, SSBs using inorganic SEs suffer from contact issues among the different cell components, leading to diminished charge percolation pathways in composite electrodes and (chemo)mechanical degradation due to electrode breathing during cycling, which in turn negatively affect capacity retention.[5] Developing advanced SEs requires to simultaneously increase both ionic conductivity and (electro)chemical stability while tailoring the (chemo)mechanical compatibility with the active and inactive electrode materials.

Current research mainly focuses on oxide-, sulfide-, halide-, and polymer-based SEs, each with distinct advantages and disadvantages. Among them, thiophosphate SEs have gained significant attention for their superionic conductivities and moderate Young's moduli (i.e. softness).[6] Certain thiophosphate SEs based on archetype crystal

structures, such as lithium argyrodites Li_6PS_5X (X = Cl, Br) and $Li_{10}GP_2S_{12}$ (LGPS), exhibit ionic conductivities that exceed those of liquid electrolytes,[7–9] making them attractive for SSB applications (considering the tortuosity of Li percolation pathways in solid electrode composites). Moreover, benefiting from their soft nature, thiophosphate SEs allow for facile integration into SSBs as no sintering is required to achieve good contact with the other cell components unlike, for example, with oxide SEs.[10] Their soft nature also enables them to better accommodate volume changes during cycling. However, void formation and cracking during cycling remain issues to be solved.[11] Aside from that, thiophosphate SEs often suffer from poor (electro)chemical stability, which further exacerbates (chemo)mechanical degradation.[12] By comparison with crystalline SEs, amorphous and glass-ceramic thiophosphate SEs exhibit more flexible polyanionic frameworks, resulting in lower Young's moduli. Regardless, they usually possess rather poor ionic conductivities (~10^{-4} mS cm^{-1}).[13–15] Nevertheless, some amorphous SEs, such as $1.5Li_2S{-}P_2S_5$ and $1.5Li_2S{-}P_2S_5{-}LiI$, glasses or glass-ceramics have been reported to better accommodate the volume change of CAMs, thus reducing (chemo)mechanical degradation and improving capacity retention of SSBs during long-term cycling.[16–18] However, the limited ionic conductivity of glassy and glass-ceramic SEs remains a challenge to be addressed.

One promising strategy to enhance ionic conductivity while retaining the softness of amorphous phases is to induce controlled (partial) crystallization, aiming at glass-ceramic SEs. For instance, in the amorphous $xLi_2S{-}yP_2S_5{-}zLiI$ system, growing a small fraction of nanocrystals has been shown to significantly increase conductivity.[19,20] Unfortunately, reported conductivities for glass-ceramic SEs vary strongly, even for compositions and heat treatments that appear to be similar,[19–21] highlighting their sensitivity to compositional and synthetic parameters. While some highly conductive glass-ceramic SEs have been successfully developed, limited understanding of their mechanical properties (regarding compressibility and (chemo)mechanical stability) persists. In the present work, we have investigated a series of glass-ceramic lithium SEs with the general formula $4.25Li_2S{-}0.75P_2S_5{-}1.5SiS_2{-}xLiI$ (i.e. $Li_{8.5}Si_{1.5}P_{1.5}S_{11}$ + xLiI). Specifically, we have examined the effect that the amount of LiI introduced into the system has on phase composition, charge-transport properties, (electro)chemical stability, and (chemo)mechanical behavior. Finally, the most promising glass-ceramic SE was tested in SSBs with a layered Ni-rich oxide cathode and an indium-lithium anode.

Experimental Section

Synthesis

Precursors for synthesis, including Li_2S (99.99%, Sigma-Aldrich), P_2S_5 (99%, Sigma-Aldrich), SiS_2 (99.99%, Goodfellow), and LiI (99.999%, Sigma-Aldrich), were used as received. All materials were stored and handled in an Ar-glovebox with H_2O and O_2 levels below 0.5 ppm. The amorphous $4.25Li_2S{-}0.75P_2S_5{-}1.5SiS_2{-}x$LiI (LPSI-LT) SEs were prepared via high-energy ball milling around 1.5 g of a stoichiometric precursor mixture using an 80 mL zirconia jar and 10 zirconia balls with a diameter of 10 mm. Initially, the mixture was milled at 250 rpm for 1 h and subsequently at 450 rpm for 12 h in total, using 24 repetitions of 30 min milling followed by 10 min rest. To obtain the glass-ceramic $4.25Li_2S{-}0.75P_2S_5{-}1.5SiS_2{-}x$LiI (LPSI-MT) SEs, the amorphous powders (LPSI-LT) were pressed into pellets at 450 MPa, vacuum sealed in quartz ampoules (10^{-3} mbar) and annealed for 2 h at the crystallization temperature determined by DSC. A heating rate of ~100 °C min^{-1} was applied, and cooling was done via removing the sample from the furnace (natural cooling in air). To obtain well-crystallized $4.25Li_2S{-}0.75P_2S_5{-}1.5SiS_2{-}x$LiI (LPSI-HT) SEs, pellets prepared from the amorphous material (LPSI-LT) were vacuum sealed in quartz ampoules (10^{-3} mbar) and annealed at 440 °C for 8 h using a heating rate of 5 °C min^{-1} followed by natural cooling via switching off the furnace. *o*-$Li_{3+a}P_{1-a}Si_aS_4$ was synthesized by blending a stochiometric precursor mixture through high-energy milling as described above. The resulting powder was pressed into a pellet, vacuum sealed in a quartz ampoule (10^{-3} mbar) and annealed at 525 °C for 8 h (heating rate of 5 °C min^{-1}, natural cooling). *t*-$Li_{10.5}P_{1.5}Si_{1.5}S_{12}$ was obtained via annealing *o*-$Li_{3+a}P_{1-a}Si_aS_4$ at 525 °C for 90 h.

Characterization

Differential scanning calorimetry. DSC measurements were conducted under Ar flow (20 mL min^{-1}) using a NETZSCH DSC 204 F1 Phoenix. Around 10 mg of LPSI-LT was sealed in an alumina crucible and heated from 25 to 400 °C at a rate of 5 °C min^{-1}.

X-ray diffraction. Powder samples were sealed in borosilicate capillaries (0.68 mm inner diameter and 0.01 mm wall thickness, Hilgenberg) under Ar atmosphere. XRD data was acquired on a STOE Stadi-P diffractometer with a DECTRIS MYTHEN 1K strip detector in Debye-Scherrer geometry. The instrument utilizes a Mo anode to generate X-rays of wavelength λ = 0.70926 Å. To determine the amorphous fraction

present in the samples, a certain amount of silicon powder (SRM 640F, NIST) as an internal standard was added. Rietveld refinement analysis was performed using the software FullProf Suite (Version 2023).

Scanning electron microscopy (SEM). SEM imaging was performed using a LEO 1530 microscope (Zeiss) equipped with a field emission gun and operated at an accelerating voltage of 10 kV.

Temperature-dependent ^{7}Li pulsed field gradient nuclear magnetic resonance spectroscopy. ^{7}Li PFG NMR measurements were performed on a Bruker Avance spectrometer at a magnetic field of 7.05 T in the temperature range of 30–74 °C. The maximal gradient strength of the diffusion probe is 30 T/m. A stimulated-echo pulse sequence with bipolar gradients was used to suppress the effects of eddy currents.[22,23] Gradient duration and diffusion time were set to 3 and 150 ms, respectively. The recycle delay was always well above five times the spin-lattice relaxation time. All samples were measured under an Ar atmosphere in 5 mm borosilicate glass tubes.

Electrochemical impedance spectroscopy. SE powder was filled into a peek sleeve (10 mm internal diameter) and two pieces of stainless-steel rods were added on both sides. The cell was pressed at 3.5 t for 3 min. Then, EIS was performed from 0.1 Hz to 7 MHz with a 20 mV voltage amplitude at a stack pressure of around 250 MPa using a SP-200 potentiostat (BioLogic). Temperature-dependent measurements were conducted from 15 to 65 °C in a climate chamber (KB115, Binder), and sintered pellets instead of cold-pressed ones were used for LPSI-MT and LPSI-HT. Indium foil (10 mm diameter) was attached on both sides and 80 MPa external pressure was applied during the measurements.

Pressure-dependent ionic conductivity and densification measurements. About 150 mg SE powder was filled into a specialized cell (ACS-A+, Sphere Energy SAS) of diameter 8 mm able to precisely control and record the uniaxial pressure while measuring the thickness of the compacted material. Initially a pressure of around 15 MPa was applied on the SE, which was successively increased up to around 250 MPa. The powder was compressed at each individual pressure for 3 min before measuring EIS and pellet thickness. EIS data was collected twice for each applied pressure, and the thickness of pellet was recorded before and after the measurement to determine both average density and ionic conductivity.

***In situ* pressure monitoring.** A similar cell was used as described for the pressure-dependent ionic conductivity and densification measurements. The working electrode

(WE) composite was prepared by blending SE powder and Super C65 (Timcal) carbon black (3:1 weight ratio) via ball milling for 30 min at 140 rpm under an Ar atmosphere using a 80 mL jar with 10 zirconia balls of 10 mm diameter. The counter electrode (CE) composite was prepared by blending carbon-coated $Li_4Ti_5O_{12}$ (NEI Corp.), Li_6PS_5Cl (NEI Corp.), and Super C65 (3:6:1 weight ratio) following the same milling procedure as described for the WE. To assemble the cell for cyclic voltammetry (CV) measurements, around 100 mg Li_6PS_5Cl was compacted at 65 MPa to form the separator layer. Next, 20 mg WE composite and 60 mg CE composite were added on opposite sides of the separator, and the stack was finally pressed at 450 MPa for 3 min. Next, an external pressure of 80 MPa was applied to the cell, and after resting for 5 h to ensure pressure stabilization, CV measurements were performed at room temperature in a potential range of 1.35–2.75 V vs. $Li_4Ti_5O_{12}/Li_7Ti_5O_{12}$ (equivalent to about 2.9–4.3 V vs. Li^+/Li) at a sweep rate of 0.1 mV s^{-1} using a SP-200 potentiostat. The pressure evolution was monitored simultaneously.

Electrode preparation, cell assembly, and SSB testing. A 1 wt.% $LiNbO_3$ coating was applied to the $LiNi_{0.85}Co_{0.10}Mn_{0.05}O_2$ (NCM851005, BASF SE) CAM, as reported elsewhere.[24] The cathode composite was prepared by blending coated NCM851005, SE, and Super C65 in a 69.3:29.7:1.0 weight ratio via ball milling (80 mL zirconia jar with 10 zirconia balls with a diameter of 10 mm) at 140 rpm for 30 min. For SSB assembly, a customized cell setup with two stainless steel dies and a PEEK sleeve (10 mm diameter) was used. Around 100 mg SE was pressed at 62.5 MPa to form the separator layer. Next, the cathode composite (~12 mg) was spread onto the separator, and the whole stack was compacted at 440 MPa. Finally, In (9 mm diameter, 125 µm thickness, GoodFellow) and Li (6 mm diameter, 50 µm thickness, Albermarle) discs were attached to the other side of the separator. Galvanostatic charge/discharge measurements were performed under an external pressure of 81 MPa at room temperature, applying different C-rates with 1C = 190 mA g^{-1}_{NCM}. Electrochemical testing was done in the potential range between 2.28 and 3.68 V vs. In/InLi (equivalent to about 2.9–4.3 V vs. Li^+/Li) after a resting period at open-circuit voltage for 1 h using a BCS-805 battery cycler (BioLogic).

X-ray photoelectron spectroscopy. XPS was employed to examine the differences in (surface) chemical composition of LPSI-GC SE before and after cycling in SSBs. To this end, the materials were transferred under Ar atmosphere (without exposure to air) from the glovebox to the ultra-high vacuum system and further to the spectrometer, a

PHI 5000 VersaProbe equipped with a monochromatic Al K_α source ($h\nu$ = 1486.7 eV). The diameter of the X-ray illuminated area was 200 µm. Photoelectrons were collected with a pass energy of E_{pass} = 23.5 eV at electron escape angles of 45° (higher surface sensitivity) and 90° with respect to the surface normal. Because SEs are poor electronic conductors, a neutralizer equipped with both a low-voltage electron gun and a floating ion gun generating a low-energy ion beam was used to compensate for sample charging. The binding energies are referenced to the C 1s photoelectron line of the C–C bond (E_{bin} = 284.8 eV). The background of spectra was subtracted using a Shirley-type function. Peak positions and areas were determined by weighted least-squares fitting of model curves (70% Gaussian, 30% Lorentzian) to the experimental data.

Results and Discussion

Starting point of our investigations was the general composition $4.25Li_2S{-}0.75P_2S_5{-}1.5SiS_2{-}xLiI$ ($Li_{8.5}Si_{1.5}P_{1.5}S_{11} + xLiI$), with the fraction of LiI varying between $0 \leq x \leq 2$. In a first step, stochiometric precursor mixtures with different LiI contents were amorphized by high-energy ball milling (referred to as LPSI-LT), and their crystallization temperatures were subsequently determined by differential scanning calorimetry (DSC). The corresponding X-ray diffraction (XRD) patterns and DSC curves are shown in **Figure S1** (Supporting Information) and **Figure 1a**, respectively. Except for trace impurities of Li_2S detected in the sample of nominal composition $Li_{8.5}Si_{1.5}P_{1.5}S_{11}$, all SEs containing LiI were found to be fully amorphous after milling. As indicated in **Figure 1a**, LPSI-LT with x = 0 exhibited a sharp exothermic peak at about 305 °C. As the LiI content increased from x = 0 to 2, the exothermic peak temperature gradually decreased from 305 to 230 °C. In a second step, the influence of a short-term heat treatment on phase formation and ionic conductivity was investigated. To do so, each individual LPSI-LT sample was annealed for 2 h at the temperature derived from the exothermic peak in the DSC measurements. This series of samples will be referred to as LPSI-MT hereafter. The corresponding XRD patterns are depicted in **Figure 1b** and reveal the presence of reflections that can be assigned to different phases, namely orthorhombic *o*-$Li_{3+a}P_{1-a}Si_aS_4$, tetragonal *t*-$Li_{10.5}P_{1.5}Si_{1.5}S_{12}$, $Li_{4+b}P_{1-b}Si_bS_4I$, and LiI. Among these phases, partial P substitution with Si may occur in a limited compositional range as will be discussed later. In a third step, all samples from the LPSI-LT series were annealed at 440 °C for 8 h to achieve full crystallization

(referred to LPSI-HT). The corresponding XRD patterns are shown in **Figure 1c**. The reflections can be assigned to three different phases, *o*-$Li_{3+a}P_{1-a}Si_aS_4$, *t*-$Li_{10.5}P_{1.5}Si_{1.5}S_{12}$, and $Li_{4+b}P_{1-b}Si_bS_4I$. Overall, various amorphous (LPSI-LT), glass-ceramic (LPSI-MT), and crystalline (LPSI-HT) samples, initially containing different amounts of LiI, were prepared. Depending on the annealing temperature and content of LiI, global trends in phase composition are evident. A schematic representation is given in **Figure 1d**.

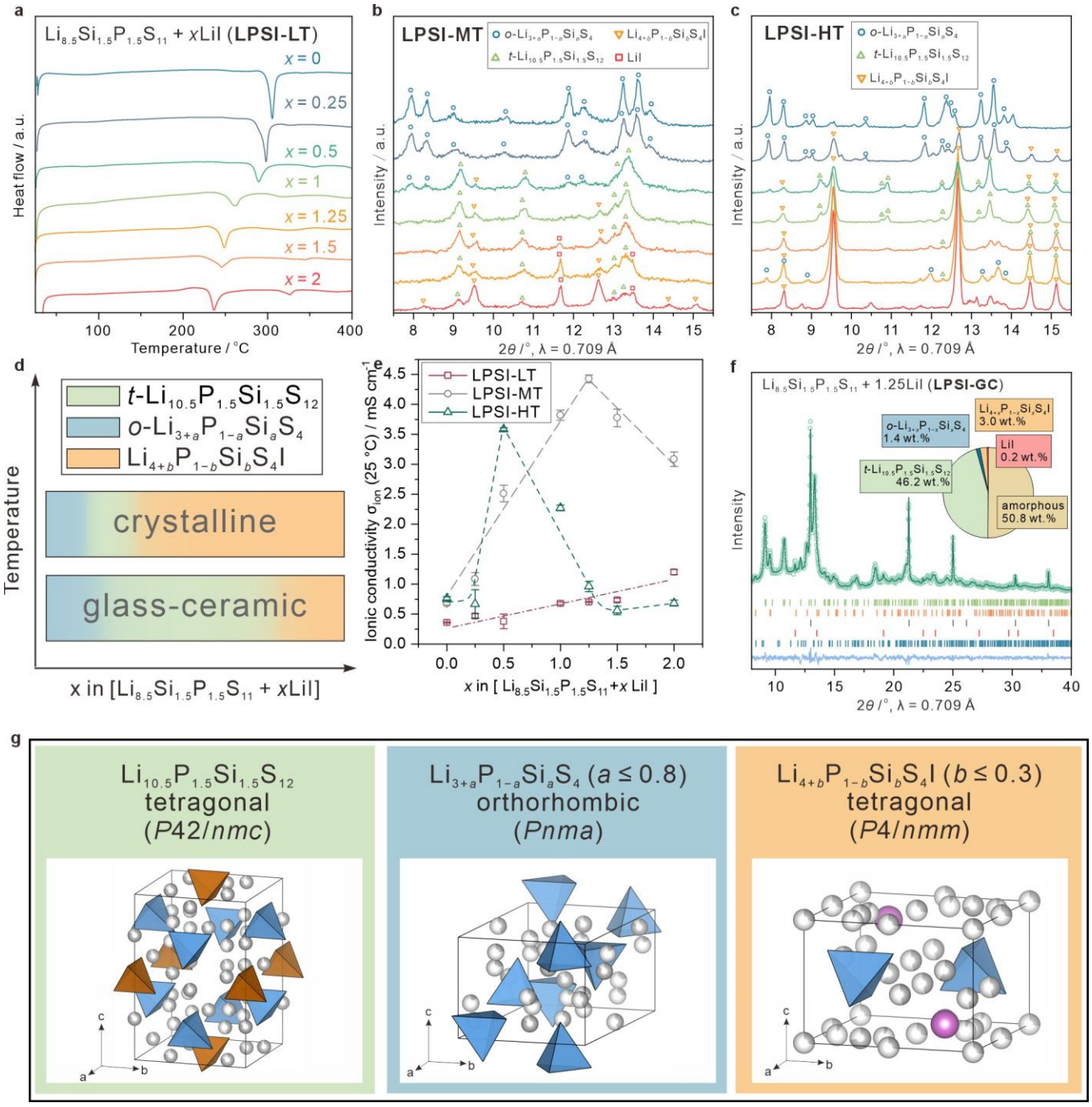

Figure 1. Synthesis and characterization of LPSI-LT, LPSI-MT, and LPSI-HT samples with the nominal composition $4.25Li_2S{-}0.75P_2S_5{-}1.5SiS_2{-}xLiI$ ($Li_{8.5}Si_{1.5}P_{1.5}S_{11}$ + *x*LiI,

with $0 \leq x \leq 2$). (a) DSC curves for LPSI-LT. XRD patterns of (b) LPSI-MT and (c) LPSI-HT. (d) Schematic representation of the effect of LiI content and annealing temperature on phase composition (only considering crystalline phases). (e) Ionic conductivities of LPSI-LT, LPSI-MT, and LPSI-HT as a function of LiI content. Conductivities were measured twice using different sample batches and any deviations are shown as error bars. (f) XRD pattern and Rietveld plot for $Li_{8.5}Si_{1.5}P_{1.5}S_{11}$ + 1.25LiI (LPSI-GC). The inset is the calculated phase composition. Open circles, green line, and blue line represent the measured, calculated, and difference data, respectively. Vertical tick marks indicate the Bragg positions for the different phases considered during the refinement. (g) Schematic representation of crystal structures for the different $Li_2S-SiS_2-P_2S_5-LiI$-based phases identified in the samples. Blue and brown tetrahedra represent mixed $[P_{1-a}Si_aS_4]^{(3+a)-}$ or $[PS_4]^{3-}$ polyanions, respectively. The space groups and range of Si substitution are indicated.

Starting from the amorphous samples ($Li_{8.5}Si_{1.5}P_{1.5}S_{11} + x$LiI), two different temperature regimes were chosen for post-treatment. The first one was determined from the temperature of the exothermic peak in the DSC measurements (between 305 and 230 °C), and the second one was set to 440 °C. For the low-temperature regime, at low LiI contents ($0 \leq x \leq 0.25$), *o*-$Li_{3+x}P_{1-x}Si_xS_4$ was found to be the major phase. When x(LiI) ≥ 0.5, the formation of *t*-$Li_{10.5}P_{1.5}Si_{1.5}S_{12}$ was observed, with the phase fraction of $Li_{4+x}P_{1-x}Si_xS_4I$ increasing with increasing x(LiI). When a high annealing temperature of 440 °C was chosen for the LPSI-LT series, again at low x(LiI) ($0 \leq x \leq 0.25$), *o*-$Li_{3+a}P_{1-a}Si_aS_4$ was present as the major phase. When the LiI content range is $0.5 \leq x \leq 1$, the presence of an additional *t*-$Li_{10.5}P_{1.5}Si_{1.5}S_{12}$ phase can be noted, and for x(LiI) > 1, $Li_{4+b}P_{1-b}Si_bS_4I$ was the major phase. As known from literature, the crystalline phases identified in the different samples possess varying ionic conductivities.

To follow the evolution in ionic conductivity related to the annealing temperature and/or LiI content, electrochemical impedance spectroscopy (EIS) measurements were conducted on cold-pressed pellets at room temperature. The trends in conductivity with increasing LiI content for LPSI-LT, -MT, and -HT are illustrated in **Figure 1e** (nominal composition of $Li_{8.5}Si_{1.5}P_{1.5}S_{11} + x$LiI for all samples). First of all, one can note, for the amorphous materials (LPSI-LT), increasing the LiI content leads to a slight increase in ionic conductivity from about 0.36 mS cm^{-1} for $x = 0$ to 1.20 mS cm^{-1} for $x = 2$. For the glass-ceramic materials (LPSI-MT), a different trend is apparent. For low amounts of

LiI (i.e. x = 0 and 0.25), the conductivity remains virtually identical to that of the corresponding LPSI-LT materials. However, if the LiI content is increased, a strong increase in ionic conductivity occurs, reaching a maximum of 4.4 mS cm^{-1} with x(LiI) = 1.25, followed by a decrease to about 3 mS cm^{-1}. Regarding the LPSI-HT samples, a maximum ionic conductivity of 3.6 mS cm^{-1} is observed for x(LiI) = 0.5. As the material with the nominal composition $Li_{8.5}Si_{1.5}P_{1.5}S_{11}$ + 1.25LiI showed the highest ionic conductivity after annealing at 250 °C (referred to as LPSI-GC hereafter), Rietveld analysis of XRD data was performed to quantitatively determine the phase composition (**Figure 1f**). An internal Si standard was added to also include the amorphous fraction. We found that 50.8 wt.% of this sample is present in an amorphous state, and the major crystalline phase is *t*-$Li_{10.5}P_{1.5}Si_{1.5}S_{12}$ (46.2 wt.%), alongside minor fractions of $Li_{4+b}P_{1-b}Si_bS_4I$ (3.0 wt.%), *o*-$Li_{3+a}P_{1-a}Si_aS_4$ (1.4 wt.%), and LiI (0.2 wt.%). This phase composition suggests that the iodine is incorporated to a great extent into the amorphous phase(s). Even though $Li_{4+b}P_{1-b}Si_bS_4I$ exhibits improved ionic conductivity when b = 0.3 (1.46 mS cm^{-1}) versus b = 0 (0.046 mS cm^{-1}), the samples are much less conductive than LPSI-GC. Hence, it is most likely not responsible for the relatively high ionic conductivity observed for LPSI-GC.[25,26] In contrast, the *t*-$Li_{10.5}P_{1.5}Si_{1.5}S_{12}$ phase has been reported to have an ionic conductivity ranging from 2.0 to 6.6 mS cm^{-1}.[27–29] This implies that the presence of this specific phase is primarily responsible for the ionic conductivity, which surprisingly is not diminished by the amorphous fraction.

In general, *o*-$Li_{3+a}P_{1-a}Si_aS_4$ shares the same structure with *β*-Li_3PS_4 and *β*-Li_4SiS_4 (*Pnma* space group), with Si and P co-occupying the same crystallographic site (**Figure 1g**).[30,31] It can therefore be regarded as a solid solution between *β*-Li_3PS_4 and *β*-Li_4SiS_4 for $a \leq 0.8$. However, when a = 0.5, a tetragonal phase can be formed (*t*-$Li_{10.5}P_{1.5}Si_{1.5}S_{12}$), which is isostructural with $Li_{10}GeP_2S_{12}$ (LGPS, *P*42/*nmc* space group). However, its formation seems to also strongly depend on the temperature profile during annealing. The refined lattice parameters are in good agreement with those reported in literature (**Table S1**).[27,31] This structure has two distinct Wyckoff positions for the P and Si sites, with one occupied only by P and the other by both. A minor amount of $Li_{4+b}P_{1-b}Si_bS_4I$-type phase (*P*4/*nmm* space group) was also observed, where the arrangement of tetrahedra is similar to that in *α*-Li_3PS_4, but with every second PS_4^{3-} replaced by iodine.[32] Note that P substitution with Si may also occur to some degree, positively affecting ionic conductivity. However, this has been reported

only up to $b < 0.3$.[33] From the lattice parameters for the $Li_{4+b}P_{1-b}Si_bS_4I$ phase present in the LPSI-GC sample, substantial P substitution is evident, as they match those calculated for $Li_{4.3}P_{0.7}Si_{0.3}S_4I$.[31] The same holds true for the *o*-$Li_{3+a}P_{1-a}Si_aS_4$ phase. By comparing the lattice parameters with those of related materials reported in literature, one can roughly estimate the range of substitution, $0.3 < a < 0.5$ (**Table S1**).

To confirm the hypothesis that the presence of *t*-$Li_{10.5}P_{1.5}Si_{1.5}S_{12}$ (46.2 wt.%) is responsible for the high ionic conductivity in LPSI-GC, this material was prepared in single-phase form. To this end, a stochiometric precursor mixture was amorphized via high-energy milling, pressed into a pellet, and annealed at 525 °C for 8 h. Afterwards, *o*-$Li_{3.5}P_{0.5}Si_{0.5}S_4$ was obtained, which underwent a phase transition to *t*-$Li_{10.5}P_{1.5}Si_{1.5}S_{12}$ after additional annealing for 90 h. The respective XRD patterns and Rietveld plots are shown in **Figure S2**. The room-temperature ionic conductivities determined on cold-pressed pellets were 0.6 and 7.2 mS cm^{-1} for the *o*- and *t*-phase, respectively. Collectively, the results provide evidence that the *t*-$Li_{10.5}P_{1.5}Si_{1.5}S_{12}$ phase is mainly responsible for achieving high ionic conductivities in the LPSI-GC samples.

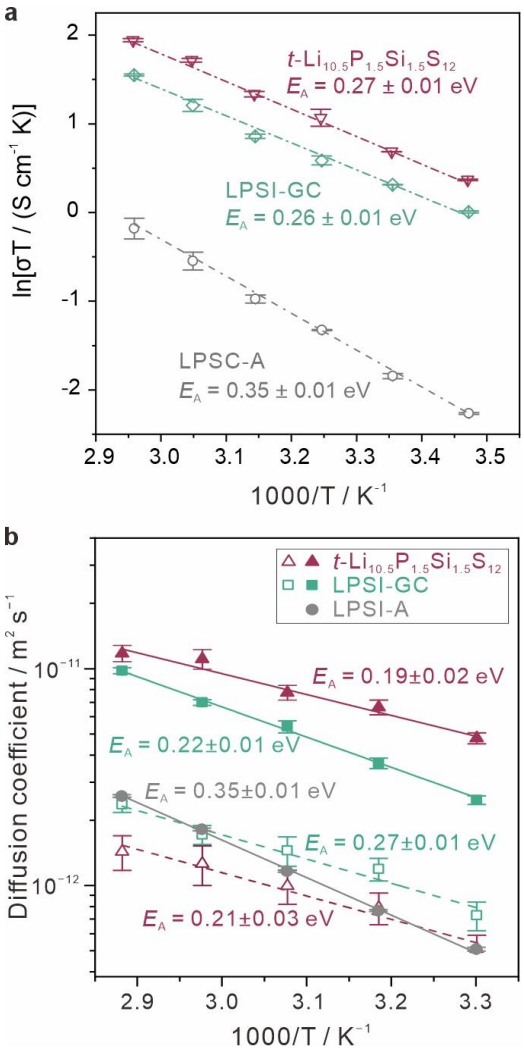

Figure 2. Arrhenius plots for (a) ionic conductivity determined by temperature-dependent EIS. Conductivities were determined twice using different sample batches and any deviations are shown as error bars. (b) ^{7}Li PFG NMR spectroscopy measurements for LPSI-A, LPSI-GC, and single-phase *t*-$Li_{10.5}P_{1.5}Si_{1.5}S_{12}$. Corresponding activation energies for Li-ion diffusion are indicated.

As the LPSI-GC sample was identified as the one possessing the highest conductivity, detailed characterizations of the transport characteristics were performed and the results compared with those for the corresponding amorphous precursor material (referred to as LPSI-A) and the single-phase *t*-$Li_{10.5}P_{1.5}Si_{1.5}S_{12}$ (LPSI-A and LPSI-GC having a similar nominal composition of $Li_{8.5}Si_{1.5}P_{1.5}S_{11}$ + 1.25LiI). At first, temperature-dependent EIS measurements (from 15 to 65 °C) were conducted on the three samples. The respective Nyquist plots can be found in **Figure S3**. The Arrhenius plots of the ionic conductivities are displayed in **Figure 2a**. For LPSI-A, an ionic conductivity of 0.7 mS cm^{-1} at 25 °C and an activation energy for conduction of 0.35 eV were determined. Upon inducing partial crystallization, meaning transforming LPSI-A into LPSI-GC, the room-temperature ionic conductivity was found to increase by a factor of about 6 to 4.4 mS cm^{-1}, while E_A decreased to 0.26 eV. The single-phase *t*-$Li_{10.5}P_{1.5}Si_{1.5}S_{12}$ reference material exhibited an ionic conductivity of 7.2 mS cm^{-1} at 25 °C and an activation energy of 0.27 eV.

To further investigate the Li-ion dynamics, ^{7}Li pulsed field gradient (PFG) nuclear magnetic resonance (NMR) spectroscopy measurements were performed over a temperature range from 30 to 74 °C. The damping of echo intensity with increasing gradient strength is presented in **Figure S4**. The Stejskal-Tanner equation was used to fit the data and extract the Li-ion diffusion coefficient, D_{Li}.[34] Arrhenius plots of the temperature-dependent lithium diffusion coefficient for LPSI-A, LPSI-GC, and *t*-$Li_{10.5}P_{1.5}Si_{1.5}S_{12}$ are displayed in **Figure 2b**. For LPSI-A, a fitting model assuming a Gaussian distribution of the diffusion coefficient was employed. The measured lithium diffusion coefficient was $5.10 \cdot 10^{-13}$ m^2 s^{-1} at 30 °C. The activation energy was 0.35 eV, closely matching that determined by EIS. For LPSI-GC, the experimental data was fitted with contributions to the diffusive motion given by the Kärger equation for slowly exchanging phases.[35] This fit describes the experimental results better than a single-component model, suggesting the presence of two conducting (amorphous/crystalline) phases (see also supplementary discussions). The signal fractions of the two

components are given in **Table S2**. Lithium diffusion coefficients of $7.62 \cdot 10^{-13}$ m^2 s^{-1} and $2.62 \cdot 10^{-12}$ m^2 s^{-1} were obtained at 30 °C, with activation energies of 0.27 and 0.22 eV resulting from a major and a minor contribution in the data fitting, respectively. The contribution with slower dynamics can likely be attributed to the amorphous phase (50.8 wt.%) and that with faster dynamics to the *t*-$Li_{10.5}P_{1.5}Si_{1.5}S_{12}$ phase (46.2 wt.%). Activation energies for both contributions are in the range of values deduced from temperature-dependent EIS measurements. To corroborate that the fast ion dynamics can indeed be ascribed to the presence of *t*-$Li_{10.5}P_{1.5}Si_{1.5}S_{12}$, ^{7}Li PFG NMR spectroscopy measurements were also conducted on the single-phase material, which was synthesized as described above. Despite the relatively high annealing temperature of 525 °C, still a significant amorphous phase fraction was present. The latter has been reported to be inevitable in the synthesis of this material.[27] This is also reflected in the data fitting, clearly revealing two distinct contributions (**Figure 2b**). We assign the main contribution to the *t*-$Li_{10.5}P_{1.5}Si_{1.5}S_{12}$ phase, while the minor contribution likely stems from the amorphous side phase. The major contribution exhibits a high lithium diffusion coefficient of $4.89 \cdot 10^{-12}$ m^2 s^{-1} at 30 °C and a low activation energy of 0.19 eV, comparable to the major contribution in LPSI-GC. In contrast to LPSI-A and LPSI-GC, in the static NMR spectra in **Figure S5**, the *t*-$Li_{10.5}P_{1.5}Si_{1.5}S_{12}$ phase reveals quadrupolar satellite peaks, originating in the quadrupolar moment of the ^{7}Li nuclei, indicating a well-defined (homogeneous) crystalline structure. However, the activation energy determined by EIS is much higher than that from ^{7}Li PFG NMR spectroscopy (0.27 vs. 0.19 eV), indicating that the amorphous side phase directly affects the macroscopic transport properties probed by EIS. The activation energies and ionic conductivities determined by EIS and PFG NMR are summarized in **Table S3** (see also supplementary discussions).

In SSBs, detrimental void formation and cracking during cell assembly and/or cycling are major issues, increasing the tortuosity of ion percolation pathways and leading to isolated (inactive) CAM particles and facilitated Li dendrite penetration through the SE separator.[5,36–38] This is primarily attributed to the rigid nature of SEs; therefore the ongoing quest for developing soft glass-ceramic inorganic ion conductors with low Young's moduli.[15] Such material characteristics not only enable to better accommodate electrode volume changes upon battery operation but also better densification during cell assembly (reduced residual void space), which in turn allows to achieve high ionic conductivities just by cold pressing, i.e. without the need for additional sintering

steps.[5,14,39,40] Favorable softness of inorganic SEs is also a major reason why SSBs employing superionic thiophosphates often demonstrate superior performance compared to those relying on oxide SEs, despite poorer (electro)chemical stability of the former. Aside from the aforementioned (chemo)mechanical interplay between electrode and electrolyte materials, it has been recognized that the (electro)chemical SE decomposition can also cause volume variations due to the different molar volumes of SE and its decomposition products, thereby accelerating (chemo)mechanical failure.[16,17] In this line, we have studied the compressibility of LPSI-GC in comparison to that of *t*-$Li_{10.5}P_{1.5}Si_{1.5}S_{12}$ by determining the density and ionic conductivity as a function of applied external pressure *in situ*. **Figure 3a** shows the acquired experimental data. Starting from an unaxial pressure of 16 MPa, one can note a sudden increase in density from ρ = 1.423 g cm^{-3}, already reaching the value of the corresponding sintered pellet (ρ = 1.894 g cm^{-3}) at about 150 MPa. A similar trend is also seen in the corresponding ionic conductivity. Starting from about 1.3 mS cm^{-1}, this value reaches almost 3.8 mS cm^{-1} at 150 MPa, whereafter only a slight increase up to 4.5 mS cm^{-1} at about 250 MPa is observed. As LPSI-GC consists of 46.2 wt.% *t*-$Li_{10.5}P_{1.5}Si_{1.5}S_{12}$, similar measurements were conducted on this material. However, it contains 14.8 wt.% of an amorphous side phase, despite the elevated temperature used in the synthesis. In contrast to LPSI-GC, the *t*-$Li_{10.5}P_{1.5}Si_{1.5}S_{12}$ powder can be densified to a much lesser extent, reaching only 0.9 g cm^{-3} at 15.6 MPa (**Figure 3b**). With increasing pressure, further densification took place, reaching 1.61 g cm^{-3} at 250 MPa and exhibiting an ionic conductivity of 5.2 mS cm^{-1}. The density determined for *t*-$Li_{10.5}P_{1.5}Si_{1.5}S_{12}$ is slightly lower than that of the sintered pellet and much lower than the crystallographic density (indicating poor densification at pressures up to 250 MPa). This is likely the reason for the lower ionic conductivity measured in the densification test compared to that of the cold-pressed pellet prepared at 450 MPa (7.2 mS cm^{-1}). Overall, these results point toward favorable mechanical densification for the glass-ceramic material. This means that better densification, along with a high ionic conductivity, is already achieved at lower pressures with positive implications for cell assembly and operation.

As mentioned above, the (chemo)mechanical properties of SEs are of prime importance regarding their performance in SSBs. Not only volume changes of electrode active materials can lead to detrimental (chemo)mechanical effects, but also the those related to the formation of decomposition products can induce pressure

variations in SSB cells. To examine the (chemo)mechanical properties of the LPSI-GC material, a cell configuration was used, where cyclic voltammetry (CV) was conducted while simultaneously monitoring current flow and pressure evolution *in situ*. To exclude CAM contributions, the working electrode (WE) consisted of a mixture of SE and carbon black. To unambiguously trace pressure changes to processes occurring at the WE, the counter electrode (CE) was based on zero-strain $Li_4Ti_5O_{12}$ (LTO). CV measurements were performed in a potential window of 1.35 to 2.75 V vs. $Li_4Ti_5O_{12}/Li_7Ti_5O_{12}$ (about 2.9–4.3 V vs. Li^+/Li) at a scan rate of 0.1 mV s^{-1} (**Figure 3c**). LPSI-A and *t*-$Li_{10.5}P_{1.5}Si_{1.5}S_{12}$ were also tested for comparison, and commercially available Li_6PS_5Cl (LPSCl) was used as a benchmark SE. During the first anodic scan, the different SEs exhibited a distinct oxidation behavior. The onset and peak currents were found to be at much lower potentials for LPSI-A, indicating that it is most prone to (electro)chemical oxidation. Both LPSI-GC and *t*-$Li_{10.5}P_{1.5}Si_{1.5}S_{12}$ revealed similar onset potentials for oxidation, with the specific currents being lower than of LPSCl, showing the highest cumulative oxidation capacity. Simultaneously, a pressure drop was observed for all materials tested, which can be attributed to volume contraction upon SE decomposition. Despite being highly prone to oxidation, LPSI-A exhibited the lowest cumulative oxidation capacity and the smallest pressure drop. By contrast, LPSCl displayed a significantly larger pressure drop, nearly twice that of LPSI-GC and *t*-$Li_{10.5}P_{1.5}Si_{1.5}S_{12}$, which agrees well with its susceptibility to degradation during battery operation. Notably, LPSI-GC revealed a somewhat smaller pressure drop than *t*-$Li_{10.5}P_{1.5}Si_{1.5}S_{12}$. During the first cathodic scan, no major reduction currents were observed. Additionally, no obvious pressure changes were detected for the different SEs, suggesting that the oxidation-induced degradation and volume variations in the initial cycle are irreversible in nature. In the second cycle (**Figure S6**), (electro)chemical oxidation was significantly suppressed (except for LPSI-A), likely due to formation of a passivation layer in the initial cycle.

The stability of LPSI-GC and *t*-$Li_{10.5}P_{1.5}Si_{1.5}S_{12}$ against Li metal was also investigated. To this end, the interfacial impedance evolution of resting Li|SE|Li symmetrical cells was monitored by EIS (**Figure S7**). First, one can note that the initial resistance of the Li|LPSI-GC interface is considerably smaller than that of the Li|*t*-$Li_{10.5}P_{1.5}Si_{1.5}S_{12}$ interface. This can be attributed either to better compressibility of LPSI-GC (i.e. better contact with Li metal) or to the iodine-rich amorphous phase, which is expected to form a more stable solid electrolyte interphase (SEI), as demonstrated previously.[41–43]

However, the impedance of Li|LPSI-GC still increased over time, indicating that interfacial stability issues still persist, or in other words, that SEI growth cannot be suppressed. The same holds true for the Li|*t*-$Li_{10.5}P_{1.5}Si_{1.5}S_{12}$ interface.

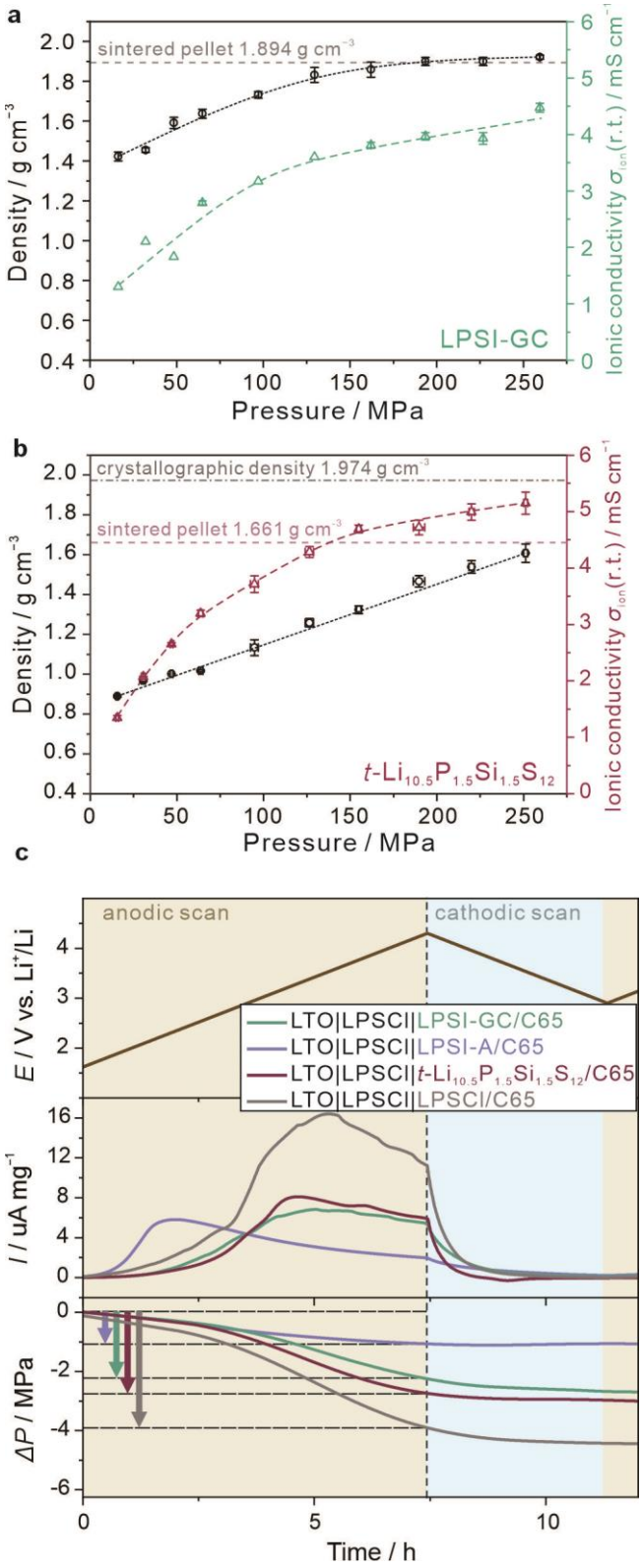

Figure 3. Densification and (chemo)mechanical behavior of LPSI-GC and LPSCl SEs. Density and ionic conductivity of (a) LPSI-GC and (b) *t*-$Li_{10.5}P_{1.5}Si_{1.5}S_{12}$ measured *in*

situ as a function of pressure. (c) Current response and pressure evolution during CV cycling of LTO|LPSCl|LPSI-GC/C65, LTO|LPSCl|LPSI-A/C65, LTO|LPSCl|*t*-$Li_{10.5}P_{1.5}Si_{1.5}S_{12}$/C65, and LTO|LPSCl|LPSCl/C65 cells.

To study the effect that SEI formation has on Li plating and stripping, the Li|SE|Li cells were cycled at a current density of 0.2 mA cm^{-2} with plating and stripping times of 1 h (**Figure S7**). Initially, minor polarizations around 20 mV were found for both SEs. Upon continuous Li plating and stripping, a strong increase in polarization was observed for *t*-$Li_{10.5}P_{1.5}Si_{1.5}S_{12}$ reaching 0.39 V after 100 h (versus 0.14 V for LPSI-GC), thus confirming the beneficial effect of iodine in stabilizing the SEI at the contact interface with Li metal.

Finally, the performance of LPSI-GC as SE was evaluated in pellet-type SSB cells using a $LiNbO_3$-coated NCM851005 (85% Ni content; loading of ~11 mg_{NCM} cm^{-2}) cathode and an In/InLi alloy anode. The first two charge-discharge profiles at C/10 rate and at room temperature are shown in **Figure 4a**. In the initial cycle, the cells delivered specific charge and discharge capacities of 225 and 193 mAh g^{-1}, respectively, resulting in a Coulomb efficiency (CE) of 86.0%. In the second cycle, a specific discharge capacity of 192 mAh g^{-1} was reached, and the CE increased to 98.7%. To assess the long-term cycling performance, similar cells were cycled at different C-rates (**Figure 4b**). Specifically, when using LPSI-GC as SE, the cells achieved specific discharge capacities of about 158, 138, and 108 mAh g^{-1} at C/2, 1C, and 2C, respectively. After 100 cycles at C/2, the cells retained 84% of their initial capacity (132 mAh g^{-1}), with an average CE of 99.4% (**Figure 4c**). For comparison, SSBs using *t*-$Li_{10.5}P_{1.5}Si_{1.5}S_{12}$ or LPSI-A as SE were also tested under the same conditions. Those with *t*-$Li_{10.5}P_{1.5}Si_{1.5}S_{12}$ were found to deliver lower specific discharge capacities of about 136, 93, and 8 mAh g^{-1} at C/2, 1C, and 2C, respectively. After 100 cycles at C/2, a capacity of 115 mAh g^{-1} was retained, corresponding to a retention of 85%, with an average CE of 99.6%. In contrast, the cells using LPSI-A achieved the lowest specific discharge capacities of about 103, 47, and 2 mAh g^{-1} at C/2, 1C, and 2C, respectively, due to inferior ionic conductivity of SE. Only 61 mAh g^{-1} were maintained after 100 cycles, with a significantly lower average CE of 99.2%, indicating severe side reactions upon cycling. Note that the fluctuating CE in the case of LPSI-GC may point toward differences in the (electro)chemical degradation behavior.

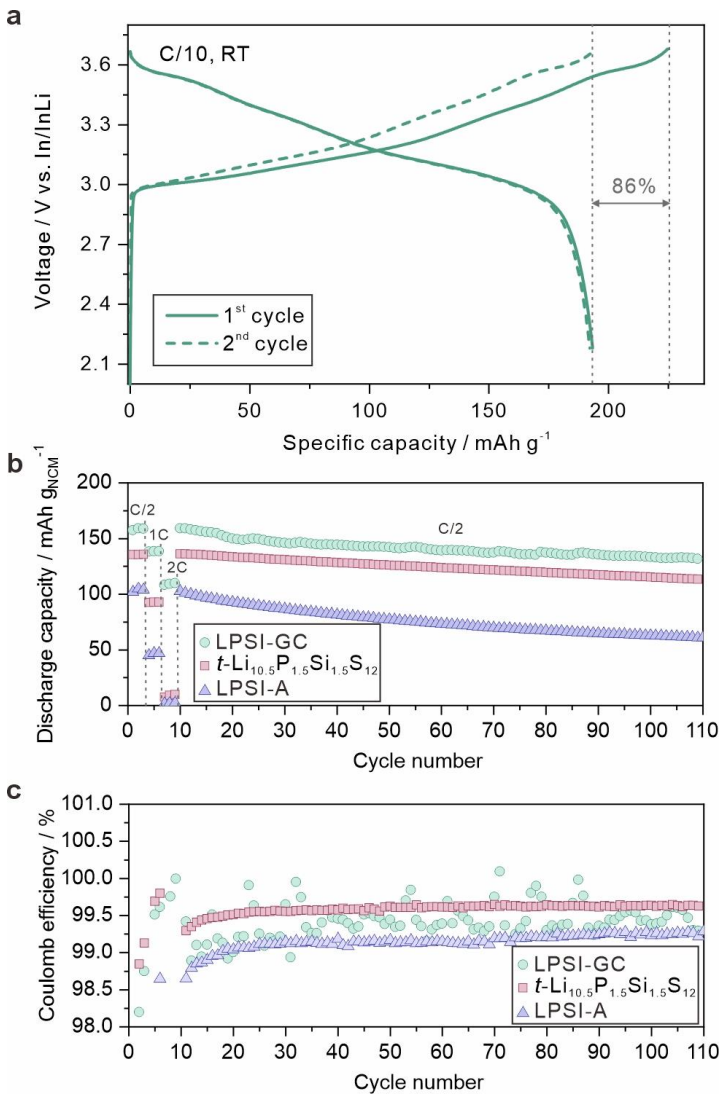

Figure 4. Assessment of LPSI-GC, LPSI-A, and *t*-$Li_{10.5}P_{1.5}Si_{1.5}S_{12}$ in SSBs with $LiNbO_3$-coated NCM851005 cathode and In/InLi anode. (a) Initial voltage profiles for LPSI-GC at C/10 rate and room temperature. (b) Rate and long-term cycling performance of cells using LPSI-GC, LPSI-A, and *t*-$Li_{10.5}P_{1.5}Si_{1.5}S_{12}$. (c) Corresponding Coulomb efficiencies.

To better understand the interfacial degradation processes, EIS measurements were performed after the first and 100th charge/discharge cycles. The corresponding Nyquist plots are shown in **Figure 5a**. The equivalent circuit used in the data fitting included contributions from the SE resistance ($R_{SE\ bulk}$), grain boundary resistance of SE ($R_{SE\ GB}$), resistance of interphases at the SE|CAM interface ($R_{SE|CAM}$), and charge-transfer resistance at both the cathode and anode sides (R_L). The calculated parameters can be found in **Table S4**. The individual resistances after the 1st and 100th cycles are compared in **Figure 5b**. After the 1st cycle, the main resistance contribution originates

from the bulk SE (21 Ω) and the charge-transfer resistance (47 Ω). This situation changes upon cycling; the resistance of interphases related to the SE/CAM contact strongly increased from 3 to 36 Ω. A similar trend is also obvious for the charge-transfer resistance, which underwent an increase from 47 to 99 Ω. These results imply that the major resistance contribution stems from the SE|CAM interface and the (electro)chemical SE decomposition.

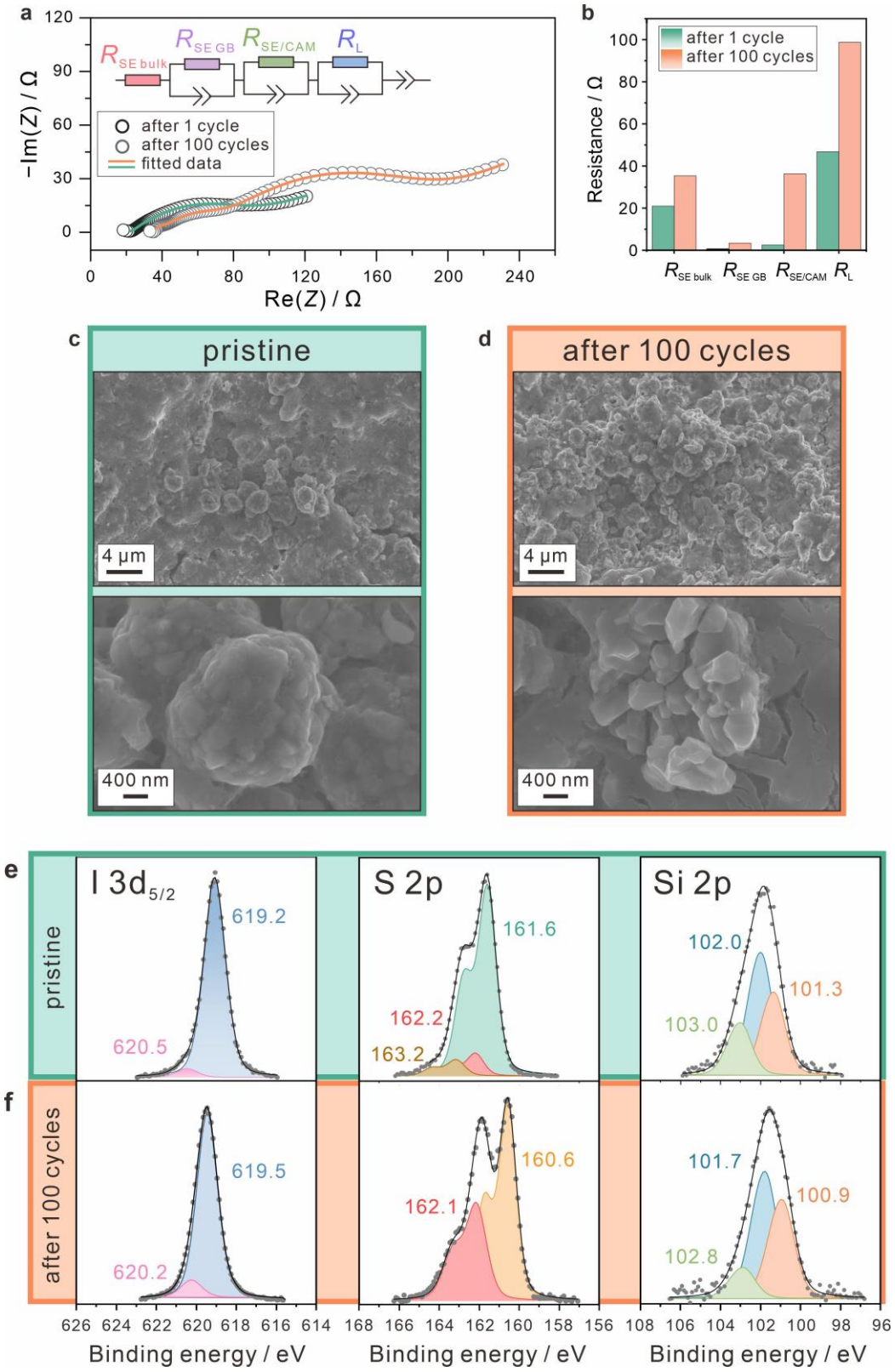

Figure 5. Analysis of LPSI-GC SE degradation after SSB cycling (100 cycles at C/2 rate). (a) Nyquist plots of the electrochemical impedance and equivalent circuit fitting results. (b) Corresponding individual resistance contributions. SEM images of the

cathode composite (c) before and (d) after cycling. (e, f) Detailed XP spectra of the SE (e) before and (f) after cycling.

Cross-sectional scanning electron microscopy (SEM) images of the cathode composite before and after cycling were taken to gain insight into morphological changes. Initially, the pelletized cathode mixture formed a dense composite structure (**Figure 5c**) with close contact between the NCM851005 secondary particles and the SE. No significant cracking was observed on the macroscopic scale after 100 cycles. However, higher-magnification SEM images revealed that while proper contact between SE and CAM was preserved, severe fracturing of the NCM851005 particles occurred. This has been shown to cause contact loss and impede charge percolation (**Figure 5d**).

To study the (electro)chemical degradation of LPSI-GC, X-ray photoelectron spectroscopy (XPS) measurements were conducted on the pristine SE and the cycled composite cathode (**Figure 5e**, **f**). The I $3d_{5/2}$ photoelectron spectrum of the pristine SE (**Figure 5e**) shows a major contribution at 619.2 eV, characteristic of ionically bond iodine.[44] The minor peak observed at 620.5 eV, slightly lower than that reported for I_2 (620.6–620.9 eV),[45,46] presumably corresponds to covalently bonded iodine species. In the S 2p spectrum of the pristine SE, a major doublet contribution centered at 161.6 eV confirms the presence of PS_4^{3-} polyanions in the *t*-$Li_{10.5}P_{1.5}Si_{1.5}S_{12}$ phase of LPSI-GC. In addition, the minor doublets at binding energies of 162.2 and 163.2 eV are indicative of P−$[S]_n$−P and S−S species, such as $P_2S_7^{4-}$ and/or $P_2S_6^{4-}$, originating from the amorphous phase fraction.[47,48] After cycling, virtually no differences in the XP spectra were visible, suggesting that major changes in the local chemical environment of iodine can be ruled out (**Figure 5f**). In contrast, notable changes were evident in the S 2p photoelectron spectrum, pointing toward two chemical states at 160.6 and 162.1 eV. The one at the lower binding energy can be assigned to Li_2S, and the one at higher binding energy is associated the formation of lithium polysulfides Li_2S_x ($2 < x < 8$).[49] This indicates that LPSI-GC undergoes severe (electro)chemically-induced transformations, leading to a rearrangement of (poly)anions in the SE. In particular, PS_4^{3-} is converted (reduction) into $P_2S_6^{4-}$ and S^{2-} during SSB operation through the following reaction, $2PS_4^{3-} + 2e^- \rightarrow P_2S_6^{4-} + 2S^{2-}$.[47] Regarding the Si 2p photoelectron spectra, three chemical states were visible for the pristine SE (**Figure 5e**). That at 101.3 eV suggests the presence of SiS_4^{4-}, stemming from the *t*-$Li_{10.5}P_{1.5}Si_{1.5}S_{12}$ phase. The peak centered at 102.0 eV can be attributed to siloxanes.[50] However, we assume

that it is rather related to the formation of S−Si−S bonds (bridging polyhedral) in the amorphous phase fraction. The Si 2p peak at 103.0 eV points toward the presence of some Si−O type impurities in the sample.[51] Upon cycling, only minor changes in the Si 2p spectra occurred (**Figure 5f**). Note that the P 2p photoelectron spectrum of the pristine LPSI-GC displays major and minor components centered at 132.0 and 132.9 eV, respectively (**Figure S8**), which can be assigned to the PS_4^{3-} units and presumably to phosphorus in the bridged thiophosphate polyanions of the amorphous phase(s).[48,52] However, after cycling, no P 2p signal could be detected, further corroborating the severe (electro)chemical decomposition of the LPSI-GC SE during cycling, i.e. depletion of phosphorus from the cathode composite facing the current collector due to interphase formation.

Conclusions

In this work, a series of quasi-quaternary Li-ion conducting sulfide-based solid electrolytes (SEs) with different amounts of incorporated LiI, namely $Li_{8.5}Si_{1.5}P_{1.5}S_{11}$ + *x*LiI (i.e. $4.25Li_2S{-}0.75P_2S_5{-}1.5SiS_2{-}$*x*LiI) with $0 \leq x \leq 2$, was successfully prepared. Initially, the materials were amorphized via high-energy milling, followed by annealing either at the crystallization temperature determined by DSC or at 440 °C. We find that a maximum room-temperature ionic conductivity of 4.4 mS cm^{-1} is achieved for the glass-ceramic SE of nominal composition $Li_{8.5}Si_{1.5}P_{1.5}S_{11}$ + 1.25LiI (LPSI-GC) after annealing at 250 °C. This high ionic conductivity is likely due to the presence of *t*-$Li_{10.5}P_{1.5}Si_{1.5}S_{12}$ (46 wt.%), in addition to amorphous phase(s) (51 wt.%), as also corroborated by complementary temperature-dependent electrochemical impedance spectroscopy (EIS) and ^{7}Li pulsed field gradient (PFG) nuclear magnetic resonance (NMR) spectroscopy. We further demonstrate that the presence of a significant amorphous side fraction gives rise to favorable (chemo)mechanical properties. If implemented in bulk-type all-solid-state batteries with a Ni-rich cathode and an In/InLi anode, LPSI-GC enables stable cycling, despite severe (electro)chemical decomposition as evidenced by post-mortem X-ray photoelectron spectroscopy (XPS) and EIS analysis. In conclusion, our findings highlight the potential of glass-ceramic sulfide SEs as a promising platform for developing next-generation SSBs by offering the opportunity to tailor conductivity, mechanical properties, and (electro)chemical stability.

Associated Content

Supporting Information

Supplementary discussions, additional XRD patterns, Rietveld refinement plots, EIS spectra, ^{7}Li PFG NMR results, CV curves, P 2p spectrum, and tables summarizing lattice parameters of various SEs, signal fractions from fitting the temperature-dependent PFG NMR data, EIS- and PFG NMR-derived activation energies and ionic conductivities, and EIS fitting parameters.

Notes

The authors declare no competing financial interest.

Acknowledgements

F.S. and J.Y. are grateful to the German Federal Ministry of Education and Research (BMBF) for funding within the project MELLi (03XP0447). This work was partially supported by Sphere Energy SAS and BASF SE.

References

(1) Schmaltz, T.; Hartmann, F.; Wicke, T.; Weymann, L.; Neef, C.; Janek, J. A Roadmap for Solid-State Batteries. *Adv. Energy Mater.* **2023**, *13*, 2301886.

(2) Cao, D.; Sun, X.; Wang, Y.; Zhu, H. Bipolar Stackings High Voltage and High Cell Level Energy Density Sulfide Based All-Solid-State Batteries. *Energy Storage Mater.* **2022**, *48*, 458–465.

(3) Liu, L.; Xu, J.; Wang, S.; Wu, F.; Li, H.; Chen, L. Practical Evaluation of Energy Densities for Sulfide Solid-State Batteries. *eTransportation* **2019**, *1*, 100010.

(4) Yang, X.; Luo, J.; Sun, X. Towards High-Performance Solid-State Li–S Batteries: From Fundamental Understanding to Engineering Design. *Chem. Soc. Rev.* **2020**, *49*, 2140–2195.

(5) Koerver, R.; Zhang, W.; Biasi, L. de; Schweidler, S.; O. Kondrakov, A.; Kolling, S.; Brezesinski, T.; Hartmann, P.; G. Zeier, W.; Janek, J. Chemo-Mechanical Expansion of Lithium Electrode Materials – on the Route to Mechanically Optimized All-Solid-State Batteries. *Energy Environ. Sci.* **2018**, *11*, 2142–2158.

(6) Famprikis, T.; Canepa, P.; Dawson, J. A.; Islam, M. S.; Masquelier, C. Fundamentals of Inorganic Solid-State Electrolytes for Batteries. *Nat. Mater.* **2019**, *18*, 1278–1291.

(7) Lin, J.; Cherkashinin, G.; Schäfer, M.; Melinte, G.; Indris, S.; Kondrakov, A.; Janek, J.; Brezesinski, T.; Strauss, F. A High-Entropy Multicationic Substituted Lithium Argyrodite Superionic Solid Electrolyte. *ACS Mater. Lett.* **2022**, *4*, 2187–2194.
(8) Kamaya, N.; Homma, K.; Yamakawa, Y.; Hirayama, M.; Kanno, R.; Yonemura, M.; Kamiyama, T.; Kato, Y.; Hama, S.; Kawamoto, K.; Mitsui, A. A Lithium Superionic Conductor. *Nat. Mater.* **2011**, *10*, 682–686.
(9) Kato, Y.; Hori, S.; Saito, T.; Suzuki, K.; Hirayama, M.; Mitsui, A.; Yonemura, M.; Iba, H.; Kanno, R. High-Power All-Solid-State Batteries Using Sulfide Superionic Conductors. *Nat. Energy* **2016**, *1*, 1–7.
(10) Sakuda, A.; Hayashi, A.; Tatsumisago, M. Sulfide Solid Electrolyte with Favorable Mechanical Property for All-Solid-State Lithium Battery. *Sci. Rep.* **2013**, *3*, 2261.
(11) Liu, B.; Pu, S. D.; Doerrer, C.; Spencer Jolly, D.; House, R. A.; Melvin, D. L. R.; Adamson, P.; Grant, P. S.; Gao, X.; Bruce, P. G. The Effect of Volume Change and Stack Pressure on Solid-State Battery Cathodes. *SusMat* **2023**, *3*, 721–728.
(12) Oh, G.; Hirayama, M.; Kwon, O.; Suzuki, K.; Kanno, R. Bulk-Type All Solid-State Batteries with 5 V Class $LiNi_{0.5}Mn_{1.5}O_4$ Cathode and $Li_{10}GeP_2S_{12}$ Solid Electrolyte. *Chem. Mater.* **2016**, *28*, 2634–2640.
(13) Garcia-Mendez, R.; Smith, J. G.; Neuefeind, J. C.; Siegel, D. J.; Sakamoto, J. Correlating Macro and Atomic Structure with Elastic Properties and Ionic Transport of Glassy Li_2S-P_2S_5 (LPS) Solid Electrolyte for Solid-State Li Metal Batteries. *Adv. Energy Mater.* **2020**, *10*, 2000335.
(14) Kato, A.; Yamamoto, M.; Sakuda, A.; Hayashi, A.; Tatsumisago, M. Mechanical Properties of Li_2S–P_2S_5 Glasses with Lithium Halides and Application in All-Solid-State Batteries. *ACS Appl. Energy Mater.* **2018**, *1*, 1002–1007.
(15) Yang, J.; Lin, J.; Brezesinski, T.; Strauss, F. Emerging Superionic Sulfide and Halide Glass–Ceramic Solid Electrolytes: Recent Progress and Future Perspectives. *ACS Energy Lett.* **2024**, *9*, 5977–5990.
(16)Wang, S.; Zhang, W.; Chen, X.; Das, D.; Ruess, R.; Gautam, A.; Walther, F.; Ohno, S.; Koerver, R.; Zhang, Q.; Zeier, W. G.; Richter, F. H.; Nan, C.-W.; Janek, J. Influence of Crystallinity of Lithium Thiophosphate Solid Electrolytes on the Performance of Solid-State Batteries. *Adv. Energy Mater.* **2021**, *11*, 2100654.
(17) Teo, J. H.; Strauss, F.; Walther, F.; Ma, Y.; Payandeh, S.; Scherer, T.; Bianchini, M.; Janek, J.; Brezesinski, T. The Interplay between (Electro)Chemical and

(Chemo)Mechanical Effects in the Cycling Performance of Thiophosphate-Based Solid-State Batteries. *Mater. Futur.* **2022**, *1*, 015102.

(18) Strauss, F.; Teo, J. H.; Janek, J.; Brezesinski, T. Investigations into the Superionic Glass Phase of Li_4PS_4 I for Improving the Stability of High-Loading All-Solid-State Batteries. *Inorg. Chem. Front.* **2020**, *7*, 3953–3960.

(19) Bonnick, P.; Niitani, K.; Nose, M.; Suto, K.; Arthur, T. S.; Muldoon, J. A High Performance All Solid State Lithium Sulfur Battery with Lithium Thiophosphate Solid Electrolyte. *J. Mater. Chem. A* **2019**, *7*, 24173–24179.

(20) Spannenberger, S.; Miß, V.; Klotz, E.; Kettner, J.; Cronau, M.; Ramanayagam, A.; Di Capua, F.; Elsayed, M.; Krause-Rehberg, R.; Vogel, M.; Roling, B. Annealing-Induced Vacancy Formation Enables Extraordinarily High Li^+ Ion Conductivity in the Amorphous Electrolyte 0.33 LiI + 0.67 Li_3PS_4. *Solid State Ion.* **2019**, *341*, 115040.

(21) Ujiie, S.; Hayashi, A.; Tatsumisago, M. Structure, Ionic Conductivity and Electrochemical Stability of Li_2S–P_2S_5–LiI Glass and Glass–Ceramic Electrolytes. *Solid State Ion.* **2012**, *211*, 42–45.

(22) Price, W. S. Pulsed-Field Gradient Nuclear Magnetic Resonance as a Tool for Studying Translational Diffusion: Part II. Experimental Aspects. *Concepts Magn. Reson.* **1998**, *10*, 197–237.

(23) Han, K. S.; Bazak, J. D.; Chen, Y.; Graham, T. R.; Washton, N. M.; Hu, J. Z.; Murugesan, V.; Mueller, K. T. Pulsed Field Gradient Nuclear Magnetic Resonance and Diffusion Analysis in Battery Research. *Chem. Mater.* **2021**, *33*, 8562–8590.

(24) Kim, H.; Choi, H.-N.; Hwang, J.-Y.; Yoon, C. S.; Sun, Y.-K. Tailoring the Interface between Sulfur and Sulfide Solid Electrolyte for High-Areal-Capacity All-Solid-State Lithium–Sulfur Batteries. *ACS Energy Lett.* **2023**, *8*, 3971–3979.

(25) Poulsen, F. W. Ionic Conductivity of Solid Lithium Iodide and Its Monohydrate. *Solid State Ion.* **1981**, *2*, 53–57.

(26) Strauss, F.; Lin, J.; Karger, L.; Weber, D.; Brezesinski, T. Probing the Lithium Substructure and Ionic Conductivity of the Solid Electrolyte Li_4PS_4I. *Inorg. Chem.* **2022**, *61*, 5885–5890.

(27) Harm, S.; Hatz, A.-K.; Moudrakovski, I.; Eger, R.; Kuhn, A.; Hoch, C.; Lotsch, B. V. Lesson Learned from NMR: Characterization and Ionic Conductivity of LGPS-like Li_7SiPS_8. *Chem. Mater.* **2019**, *31*, 1280–1288.

(28) Whiteley, J. M.; Woo, J. H.; Hu, E.; Nam, K.-W.; Lee, S.-H. Empowering the Lithium Metal Battery through a Silicon-Based Superionic Conductor. *J. Electrochem. Soc.* **2014**, *161*, A1812.

(29) Schneider, C.; Schmidt, C. P.; Neumann, A.; Clausnitzer, M.; Sadowski, M.; Harm, S.; Meier, C.; Danner, T.; Albe, K.; Latz, A.; Wall, W. A.; Lotsch, B. V. Effect of Particle Size and Pressure on the Transport Properties of the Fast Ion Conductor T-Li_7SiPS_8. *Adv. Energy Mater.* **2023**, *13*, 2203873.

(30) Murayama, M.; Kanno, R.; Irie, M.; Ito, S.; Hata, T.; Sonoyama, N.; Kawamoto, Y. Synthesis of New Lithium Ionic Conductor Thio-LISICON—Lithium Silicon Sulfides System. *J. Solid State Chem.* **2002**, *168*, 140–148.

(31) Zhou, L.; Assoud, A.; Shyamsunder, A.; Huq, A.; Zhang, Q.; Hartmann, P.; Kulisch, J.; Nazar, L. F. An Entropically Stabilized Fast-Ion Conductor: $Li_{3.25}[Si_{0.25}P_{0.75}]S_4$. *Chem. Mater.* **2019**, *31*, 7801–7811.

(32) Sedlmaier, S. J.; Indris, S.; Dietrich, C.; Yavuz, M.; Dräger, C.; von Seggern, F.; Sommer, H.; Janek, J. Li_4PS_4I: A Li^+ Superionic Conductor Synthesized by a Solvent-Based Soft Chemistry Approach. *Chem. Mater.* **2017**, *29*, 1830–1835.

(33) Ramos, E. P.; Kim, N.; Assoud, A.; Kochetkov, I.; Wan, L.; Nazar, L. F. Triggering Fast Lithium Ion Conduction in Li_4PS_4I. *ACS Mater. Lett.* **2023**, *5*, 144–154.

(34) Stejskal, E. O.; Tanner, J. E. Spin Diffusion Measurements: Spin Echoes in the Presence of a Time-Dependent Field Gradient. *J. Chem. Phys.* **1965**, *42*, 288–292.

(35) Jiang, P.; Zhou, H.; Song, S.; Suzuki, K.; Watanabe, K.; Yamaguchi, Y.; Matsui, N.; Hori, S.; Kanno, R.; Hirayama, M. A Composite Cathode with a Three-Dimensional Ion/Electron-Conducting Structure for All-Solid-State Lithium–Sulfur Batteries. *Commun. Mater.* **2024**, *5*, 1–14.

(36) Bielefeld, A.; Weber, D. A.; Janek, J. Modeling Effective Ionic Conductivity and Binder Influence in Composite Cathodes for All-Solid-State Batteries. *ACS Appl. Mater. Interfaces* **2020**, *12*, 12821–12833.

(37) Lewis, J. A.; Tippens, J.; Cortes, F. J. Q.; McDowell, M. T. Chemo-Mechanical Challenges in Solid-State Batteries. *Trends Chem.* **2019**, *1*, 845–857.

(38) Zhong, Y.; Zhang, X.; Zhang, Y.; Jia, P.; Xi, Y.; Kang, L.; Yu, Z. Understanding and Unveiling the Electro-Chemo-Mechanical Behavior in Solid-State Batteries. *SusMat* **2024**, *4*, e190.

(39) Hikima, K.; Totani, M.; Obokata, S.; Muto, H.; Matsuda, A. Mechanical Properties of Sulfide-Type Solid Electrolytes Analyzed by Indentation Methods. *ACS Appl. Energy Mater.* **2022**, *5*, 2349–2355.
(40) Ke, X.; Wang, Y.; Ren, G.; Yuan, C. Towards Rational Mechanical Design of Inorganic Solid Electrolytes for All-Solid-State Lithium Ion Batteries. *Energy Storage Mater.* **2020**, *26*, 313–324.
(41) Duan, C.; Cheng, Z.; Li, W.; Li, F.; Liu, H.; Yang, J.; Hou, G.; He, P.; Zhou, H. Realizing the Compatibility of a Li Metal Anode in an All-Solid-State Li−S Battery by Chemical Iodine–Vapor Deposition. *Energy Environ. Sci.* **2022**, *15*, 3236–3245.
(42) Han, F.; Yue, J.; Zhu, X.; Wang, C. Suppressing Li Dendrite Formation in Li_2S-P_2S_5 Solid Electrolyte by LiI Incorporation. *Adv. Energy Mater.* **2018**, *8*, 1703644.
(43) Bron, P.; Roling, B.; Dehnen, S. Impedance Characterization Reveals Mixed Conducting Interphases between Sulfidic Superionic Conductors and Lithium Metal Electrodes. *J. Power Sources* **2017**, *352*, 127–134.
(44) Moulder, J. F.; Chastain, J. *Handbook of X-Ray Photoelectron Spectroscopy: A Reference Book of Standard Spectra for Identification and Interpretation of XPS Data*; Physical Electronics Division, Perkin-Elmer Corporation, **1992**.
(45) Guo, X.; Yu, J.; Ma, L.; Yuan, J.; Guo, T.; Ma, Y.; Xiao, S.; Bai, J.; Zhou, B. Covalent Organic Polyrotaxanes Based on β-Cyclodextrin for Iodine Capture. *RSC Adv.* **2024**, *14*, 30077–30083.
(46) Dietrich, P. M.; Kjærvik, M.; Willneff, E. A.; Unger, W. E. S. In-Depth Analysis of Iodine in Artificial Biofilm Model Layers by Variable Excitation Energy XPS and Argon Gas Cluster Ion Sputtering XPS. *Biointerphases* **2022**, *17*, 031002.
(47) Koerver, R.; Walther, F.; Aygün, I.; Sann, J.; Dietrich, C.; Zeier, W. G.; Janek, J. Redox-Active Cathode Interphases in Solid-State Batteries. *J. Mater. Chem. A* **2017**, *5*, 22750–22760.
(48) Auvergniot, J.; Cassel, A.; Ledeuil, J.-B.; Viallet, V.; Seznec, V.; Dedryvère, R. Interface Stability of Argyrodite Li_6PS_5Cl toward $LiCoO_2$, $LiNi_{1/3}Co_{1/3}Mn_{1/3}O_2$, and $LiMn_2O_4$ in Bulk All-Solid-State Batteries. *Chem. Mater.* **2017**, *29*, 3883–3890.
(49) Wu, Y.; Momma, T.; Ahn, S.; Yokoshima, T.; Nara, H.; Osaka, T. On-Site Chemical Pre-Lithiation of S Cathode at Room Temperature on a 3D Nano-Structured Current Collector. *J. Power Sources* **2017**, *366*, 65–71.
(50) Riegger, L. M.; Otto, S.-K.; Sadowski, M.; Jovanovic, S.; Kötz, O.; Harm, S.; Balzat, L. G.; Merz, S.; Burkhardt, S.; Richter, F. H.; Sann, J.; Eichel, R.-A.; Lotsch, B. V.;

Granwehr, J.; Albe, K.; Janek, J. Instability of the Li_7SiPS_8 Solid Electrolyte at the Lithium Metal Anode and Interphase Formation. *Chem. Mater.* **2022**, *34*, 3659–3669.
(51) Won, S.-J.; Suh, S.; Huh, M. S.; Kim, H. J. High-Quality Low-Temperature Silicon Oxide by Plasma-Enhanced Atomic Layer Deposition Using a Metal–Organic Silicon Precursor and Oxygen Radical. *IEEE Electron Device Lett.* **2010**, *31*, 857–859.
(52) Dietrich, C.; Koerver, R.; Gaultois, M. W.; Kieslich, G.; Cibin, G.; Janek, J.; Zeier, W. G. Spectroscopic Characterization of Lithium Thiophosphates by XPS and XAS – a Model to Help Monitor Interfacial Reactions in All-Solid-State Batteries. *Phys. Chem. Chem. Phys.* **2018**, *20*, 20088–20095.

TOC Graphic

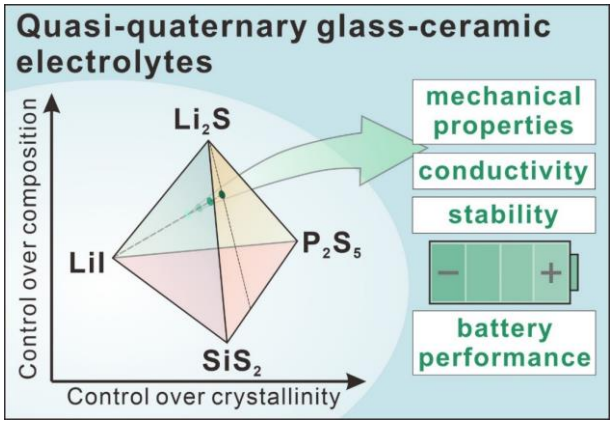
Quasi-quaternary glass-ceramic electrolytes
Li2S
LiI
P2S5
SiS2
Control over composition
Control over crystallinity
mechanical properties
conductivity
stability
battery performance